

Bio-Inspired Interfaces for Easy-to-Recycle Lithium-Ion Batteries

Congrui Jin^{1*}, Zhen Yang², Jianlin Li³, Yijing Zheng⁴, Wilhelm Pfleging^{4,5}, Tian Tang^{2*}

¹Department of Mechanical Engineering, Binghamton University, Binghamton, NY, 13902 USA

²Department of Mechanical Engineering, University of Alberta, Edmonton, AB T6G 1H9, Canada

³Energy and Transportation Science Division, Oak Ridge National Laboratory, Oak Ridge, TN, 37831 USA

⁴Karlsruhe Institute of Technology, IAM-AWP, P.O. Box 3640, 76021 Karlsruhe, Germany

⁵Karlsruhe Nano Micro Facility, H.-von-Helmholtz-Platz 1, 76344 Egg.-Leopoldshafen, Germany

*Corresponding authors: Email address: cjin@binghamton.edu (C. Jin) and ttang1@ualberta.ca (T. Tang)

Keywords: battery recycling, lithium-ion batteries, bio-inspired interfaces, directional adhesion, gecko's feet

Abstract The recycling of spent lithium-ion batteries has significant potential to benefit our society economically and environmentally as well as preserving raw materials. Although diverse process chains have been applied or under development to recycle batteries, a common, critical issue for battery recycling is the separation of the metallic current collector from the composite film of the electrode. In this study, inspired by the amazing controllable attachment and detachment ability of geckos' foot-hairs, microscale near-surface architecture is designed on the interface between the current collector and the composite film in lithium-ion batteries, so that it displays controllable and directional adhesion, i.e., enhanced adhesion can be obtained during its lifetime to cope with the substantial volume changes of the composite film upon intercalation and deintercalation, whereas during recycling, the composite layer of the electrode can be easily peeled off from the current collector in a certain direction. This study is the first application of structural adhesives for the development of easy-to-recycle lithium-ion batteries. This technology can also be extended to other electronic products to avoid an ever-growing volume of electronic waste. The fundamental understanding on the interfacial adhesion and delamination mechanisms provides a scientific footing for the realization of next-generation easy-to-recycle electronics.

1. Introduction

Lithium-ion batteries have been widely used as power sources during the past two decades due to their high energy density, high power density, low self-discharge rate, no memory effect, and quick charge acceptance.^[1-6] They are now manufactured at a rate of several million units per month, and the demand is expected to increase further with the increasing prevalence of portable electronics and electric vehicles.^[7-9] Batteries either control the lifetime of a product or are the component which needs to be replaced first. Consequently, the end-of-life batteries are becoming an environmental burden, leading to an increasing demand for spent battery collection systems.^[10]

Recent research states that, for the production of twenty million electronic vehicle batteries every year, the demand of cobalt equals to the current world mine production and will consume the current cobalt reserves in approximately sixty years, and the nickel needed for this production rate would be larger by approximately two hundred folds than today's production capacity.^[11] Although

lithium incurs only a small portion of the total cost compared with other raw materials used for battery manufacturing, there will be a serious pressure on lithium suppliers to cater to demand in the near future.^[12-15] Thus, the recycling of spent lithium-ion batteries has significant potential to benefit our society both economically and environmentally as well as preserving raw materials.^[16-20]

However, recycling technology is still in its infancy.^[21] Right now it does not make any economic sense to recycle the lithium-ion batteries. Although diverse process chains have been applied or under development to recycle batteries, a common, critical issue for battery recycling is the separation between the composite film and the metallic current collector.^[22,23] A lithium-ion battery consists of a cathode, an anode, an organic electrolyte and a separator. The cathode is typically made up of aluminum foil coated by a thin layer of powdered lithium transition metal oxide, whereas the anode consists of copper foil coated by a thin layer of graphite.^[5,9] Each electrode also contains a polymer binder, which yields significant adhesion to the current collector and holds the active material particles together, providing the key function for a good interface property to maintain the electrode integrity of lithium-ion batteries.

To separate the composite film from the metallic current collector, usually an intensive milling step is applied during recycling. Although the mechanical stressing loosens the composite film from the foil, it typically leads to smaller foil fragments which need to be screened. Other methods have also been proposed, such as dissolving the electrode in a solvent,^[24] applying thermal decomposition to the electrode to weaken the interfacial adhesion,^[25,26] and more recently, using a combined thermal and mechanical process to separate the metallic current collector from the composite film.^[27] Despite the feasibility and sophistication of those proposed techniques, they are complicated to implement and still require significant time and resources.

On the other hand, since the delamination between the metallic current collector and the composite film is usually regarded as one of the important causes of capacity decay and battery failure, many strategies have been developed and adopted in battery manufacturing to increase the adhesion strength of the interface between the metallic current collector and the composite film, such as using a highly adhesive binder,^[28-30] carbon coating to remove the native oxide layer and modify surface hydrophobicity,^[31] building an array of nano-rods to increase the surface area of the current collector,^[32] and roughening of the current collector surface by electrolytic deposition^[33] or laser ablation.^[34] Those techniques indeed lead to enhanced battery lifetime, however, they also make the battery recycling much more challenging. In particular, the recent trend to realize thick-film electrodes,^[35] three-dimensional electrodes,^[35] and silicon-based electrodes for high energy and high power applications^[36] have implications for an urgent need for improved adhesion between the metallic current collector and the composite film, which could further complicate the battery recycling process.

Challenges of battery technologies have been traditionally understood in terms of electrochemistry. Mechanical aspect has been regarded as a secondary consideration in the design spectrum. However, as conventional methods are not satisfactory to assure the function of the interface between the metallic current collector and the composite film, i.e., to display superior adhesion to effectively combat mechanical delamination during its lifetime, and at the same time, to be easily separated at the end of its life during recycling, expert knowledge in contact mechanics, especially

in adhesion and delamination mechanisms of interfaces, is becoming essential for the development of next-generation high-performance easy-to-recycle batteries. Innovative research and revolutionary discoveries of new materials, new structures, and new interfacial designs are urgently needed. Such an emerging field provides an opportunity for electrochemists and mechanicians to build collaborations, enabling the battery manufacturing industry to pursue new design philosophies for both enhanced battery life performance and increased recyclability.

The goal of this study is to design microscale near-surface architecture on the interface between the current collector and the composite film so that it displays controllable and directional adhesion, i.e., enhanced adhesion is obtained during its lifetime to cope with the substantial volume changes of the composite film upon intercalation and deintercalation, whereas during recycling, the composite film can be easily peeled off from the current collector in a certain direction. This idea was originally inspired by the controllable and directional adhesion exhibited by the geckos' foot-hairs.^[37-59] Geckos are considered as one of the most agile climbers in nature. They possess controllable attachment and detachment capabilities on a wide range of smooth and rough surfaces, mainly due to the angled and hierarchical micro-/nano-scale fibrillar structures on their feet.^[37] These micro-/nano-structures can exhibit repeatable adhesive strengths up to 200 kPa on even molecularly smooth surfaces.^[38] The origin of the strong adhesion strength of gecko foot-hairs stems from intermolecular forces such as van der Waals forces, which exist for all surfaces and are fairly insensitive to surface chemistry.^[37] This principle suggests that evolution can lead to an effective adhesive by simply building near-surface architecture rather than by synthesizing a structure with a specialized surface chemistry. Since these discoveries, many researchers proposed innovative designs of synthetic micro-/nano-structured adhesives.^[39-50] Those adhesives are often called bio-inspired structural adhesives.

More importantly, besides the enhanced adhesion strength, biological micro-/nano-fibrillar structures also exhibit highly directional adhesion.^[51-56] For example, the adhesion and shear strength of gecko's angled fibrillar structures depends on mechanical deformations induced by vertical and lateral loading of its feet, which actively control the contact area between the structures and the substrate. Autumn et al. have shown that gecko foot-hairs possess a friction ratio of 5 to 1 comparing the "with" to "against" hair tilt directions.^[57] Structural adhesives have been designed to mimic the directionality and controllability of the biological foot-hairs. For example, Murphy et al. developed polymeric surfaces with arrays of angled microfibers with angled mushroom tips that exhibited directional shear and adhesion strength – a with-to-against shear ratio of around 5 to 1 and an amazing adhesion ratio of 35 to 1.^[59]

In this study, structural adhesives have been designed to mimic the directionality of these biological foot-hairs. Composite electrode materials are deposited on the patterned aluminum current collectors. The directional adhesion of the composite film is characterized by performing 90° peeling tests. Finite element analyses are conducted to explain adhesion measurement results and elucidate the underlying mechanisms.

2. Results and Discussion

2.1 Experimental Results

In the application of easy-to-recycle batteries, directional adhesion is desired where interface separation along different directions requires different fracture energy. Although more sophisticated structures may function better, as a proof-of-concept investigation, the simplest triangular pattern was used. In this study, two types of patterned surfaces, called Model A and Model B, were fabricated on the aluminum plates, both of which contained asymmetric right triangles separated by flat regions, but with different geometrical parameters, as shown in **Figure 1**. Totally 20 aluminum plates with patterned surfaces were fabricated, with ten for each pattern. Ten aluminum plates with flat surfaces were also fabricated, serving as a control. All the plates have the global dimension of 20 mm × 10 mm × 0.5 mm.

The fabrication of LiNi_{0.5}Mn_{0.3}Co_{0.2}O₂ (NMC532) electrodes followed the procedure which was reported previously.^[60-62] N-Methylpyrrolidone (NMP) was used as solvent. The electrodes were coated onto the aluminum plates with either patterned or flat surfaces. The composite film was composed of NMC532 particles, PVDF binders, and porous carbon black matrix.^[62] All the electrodes were not calendered, and the thickness of the composite film was approximately 50 μm ± 3 μm.

To investigate the adhesion between the aluminum substrates and the composite films, the composite films were peeled off using a universal testing machine according to the standard procedure ASTM D6862.^[63] The angle between the force direction and the interface was kept at 90° during the peeling tests. The initial part of the composite film was manually peeled off and attached to an adhesive tape, and the remaining composite film was then peeled off at a constant rate of 0.7 mm/min. For each patterned interface, the composite film was peeled off from the aluminum substrate along two different directions, as shown in **Figure 2**. The force F needed to peel the composite films from the aluminum substrates was recorded. The peel energy can be deduced from the peel force F as F/M_t with M_t being the width of the tape.^[64]

Since the triangular pattern is asymmetric, as the crack propagates from left to right, i.e., following the peeling direction 1, it travels upwards along the vertical side of the triangle, and then downwards along the hypotenuse; and as the crack propagates from right to left, i.e., following the peeling direction 2, it travels upwards along the hypotenuse, and then downwards along the vertical side. Along each direction, there is a flat region before the separation of the patterned region. The adhesion strength is expected to be different along different directions.

Figure 3 shows the results of the peel energy for Model A and Model B and each with two peeling directions, respectively. Ten different measurements were conducted for each case. Error bars represent standard deviation based on the ten measurements. The results obtained from the flat control are also presented as reference. These data were obtained from the tests in which the composite film was completely peeled off from the aluminum substrate. If the composite film was not completely removed from the aluminum substrate, the data were considered as not useful for the analysis.

The peel energy for the flat control is in the range of 22.8 N/m to 32.3 N/m. For Model A, the peel energy along the peeling direction 1 varies in the range of 103.0 N/m to 117.0 N/m, while the peel energy along the peeling direction 2 varies in the range of 116.5 N/m to 136.0 N/m. For Model B, the peel energy along the peeling direction 1 varies in the range of 63.0 N/m to 77.0 N/m, whereas

the peel energy along the peeling direction 2 varies in the range of 80.5 N/m to 98.5 N/m. Enhanced adhesion of films deposited on patterned aluminum is observed in comparison to the flat control. Most importantly, directional adhesion is observed in both Model A and Model B. For both models, the peel energy along the peeling direction 2 is larger than that along the peeling direction 1. The ratio of the peel energy along the peeling direction 2 to that along the peeling direction 1 is approximately 1.15 for Model A and 1.28 for Model B, respectively, indicating that directional adhesion is slightly stronger in Model B where $\theta = 12^\circ$ than in Model A where $\theta = 45^\circ$. In the next section, finite element analyses were performed to explain the adhesion measurement results and elucidate the underlying mechanisms.

2.2 Numerical Simulation Results

Commercial package Abaqus FEA^[65] was utilized for the finite element analysis. Two patterned interface models, Model A and Model B, based on the actual geometries and materials used in the experiments were simulated, respectively. The numerical models created with the plane strain assumption are two-dimensional. The dimensions of the numerical models, as listed in **Table 1**, are consistent with the experimental models except for the length L , which is much smaller in numerical simulation to reduce computational cost. The materials used in the composite film and the aluminum substrate are both assumed to be linearly elastic. The Young's modulus and the Poisson's ratio of the substrate are assumed to be 69.0 GPa and 0.13, respectively, which are typical values for the 7075 grade aluminum alloys. The composite film is assumed to be of homogenous material with the Young's modulus of 2.0 GPa and the Poisson's ratio of 0.38, respectively, which are typical values for PVDF binders.

For the two numerical models, the same loading condition is applied where the first few nodes on the top edge is subjected to a fixed displacement boundary condition, and the bottom edge is fixed in a frictionless manner. The displacement δ increases linearly from 0 to δ_0 as the numerical step n increases from 0 to n_0 , and afterwards δ remains constant. For both models, δ_0 is assumed to be 10 μm . Two opposite crack separation directions are examined numerically, as shown in **Figure 4**. It is noted that the peeling condition applied in the finite element analysis is different from that used in the experiments. The angle between the force direction and the interface was kept at 90° during the peeling experiments, but simulating 90° peeling would require extensive re-meshing which is avoided in the numerical simulation.

All the paired nodes along the interface are initially tied using the "tie" constraint from step 0 to n_0 . After the step n_0 , the paired interface nodes start being released from the "tie" constraint, one during each step. In this manner, the length of the crack is extended in the direction along which the tied nodes are released. The node releasing process does not mimic the natural crack propagation, and hence the releasing does not follow certain criteria. Rather, controlled releasing of the nodes allows us to control the length of the crack, and the energy release rate for both the patterned interface and the flat interface can be evaluated at each given crack length. During each numerical step n , the strain energy for the entire model U_n is recorded, and the energy release rate G at the crack tip can be calculated as $G = -dU / da \approx (U_n - U_{n+1}) / (a_{n+1} - a_n)$, where a_n represents the actual crack tip location at the step n . The energy release rate for patterned interfaces and flat interfaces are denoted as $G_{pattern}$ and G_{flat} , respectively. $G_{pattern}$ can be normalized by G_{flat} to obtain the energy release rate ratio R , which is defined as $R \equiv G_{pattern} / G_{flat}$. If $R < 1$, then under the same

loading condition, the patterned interface leads to reduction in G compared with the flat interface. If a crack is able to propagate along the flat interface, this reduction might cause the crack to be trapped on the patterned interface. In other words, in order to propagate the crack on the patterned interface, the external load will need to be increased for $G_{pattern}$ to reach G_{flat} . Therefore, the apparent adhesion is enhanced by the patterns. The minimum of R , denoted as R_{min} , represents the maximum reduction in $G_{pattern}$, and thus we can define an adhesion enhancement factor as $E = 1/R_{min}$, which is an important indicator of how much adhesion is enhanced compared to the flat control.

Figure 5 shows how R changes with the normalized apparent crack tip location x/λ_x for the two numerical models and each with two peeling directions, respectively. The parameter x represents the projected length of the interface onto the horizontal direction, and λ_x is defined as $\lambda_x = h/\text{tg}\theta + w$, representing the apparent or horizontally projected length of the interface in each period. The projection of any points along the vertical portion of the patterned interface onto the horizontal direction is a single point, i.e., they have the same value of x . Note that in the initial flat portion of the models, the crack has not yet reached the patterned region and therefore $R = 1$, which is excluded from the plots in Figure 5.

As can be seen from Figure 5, R deviates from 1 along the patterned surface, and there are several local minima of R . To facilitate the discussion, the first three “kinks” in the patterned region are labeled in Figure 4 where the crack propagation changes direction. They are denoted by A , B and C based on the sequence in which they are accessed by the crack tip. Subscripts 1 and 2 are used to denote different directions. For example, A_1 corresponds to the first “kink” accessed by the crack tip when the crack is extended along direction 1. As seen in Figure 5(a) and Figure 5(c), during each period along the peeling direction 1, R reaches the first local minimum when the crack tip reaches A_1 . As the crack tip moves upwards along the vertical side of the triangle, R rapidly increases to very high values and reach a local maximum at B_1 . After the crack tip passes B_1 , R drops immediately and then slowly decreases to the second local minimum at C_1 . As the crack tip further advances, R first increases and then decreases to the local minimum at A_1 in the second period. The main observation along the peeling direction 1 is that for both models the R curves show two local minima during each period, one located at A_1 and the other one located at C_1 .

Along the peeling direction 2, as shown in Figure 5(b) and Figure 5(d), during the first period, when the crack tip reaches A_2 , R starts increasing from 1. As the crack tip propagates along the ramping-up surface, R increases rapidly to the local maximum located at B_2 . After the crack tip passes B_2 and propagates along the vertical-down surface, R rapidly drops and reaches a local minimum when the crack tip is near C_2 . As the crack further propagates in the flat region, R slowly increases and shows a discontinuity at A_2 in the second period. Different from the peeling direction 1, along the peeling direction 2 the R curves for both models show only one local minimum during each period, which is located along the vertical down surface near C_2 .

Further analysis is provided in **Figure 6**. Figure 6(a) and Figure 6(b) plot R_{min} , the minima of the R in each period of the pattern, against the normalized apparent crack tip location for the two models and each with two peeling directions, respectively. Since along the peeling direction 1 there are two local minima in each period, only the smaller one is extracted for the plot. It can be seen that, for model A, R_{min} always occurs near C_1 along the peeling direction 1 and near C_2 along

the peeling direction 2. For model B, R_{min} also occurs near C_2 along the peeling direction 2. However, along the peeling direction 1, R_{min} occurs near C_1 in the first two periods and near A_1 in the later three periods.

The R_{min} values are then used to calculate the adhesion enhancement factor E , as shown in Figure 6(d) and Figure 6(e). For Model A, the value of E along the peeling direction 2 varies in the range of 9.25 to 133, while the value of E along the peeling direction 1 varies in the range of 14.5 to 32.4. The value of E along the peeling direction 2 is much higher than that along the peeling direction 1 in the first period and then becomes slightly lower in later periods. For Model B, the value of E along the peeling direction 2 varies in the range of 4.01 to 110, whereas that along the peeling direction 1 varies in the range of 3.26 to 6.40. It can be seen that, the values of E obtained along two directions in Model A where $\theta = 45^\circ$ are comparable and are both higher than those in Model B, whereas in Model B where $\theta = 12^\circ$ the value of E along the peeling direction 2 is noticeably higher than that along the peeling direction 1. In other words, compared with Model B, adhesion is stronger but directional adhesion is weaker in Model A, which is consistent with the experimental results. The main difference between Model A and Model B is the angle θ , with triangles in Model A having steeper hypotenuse. Such larger slope favors crack trapping, making crack propagation in Model A to be more difficult, and hence enhancing the adhesion. On the other hand, large θ in Model A makes the E values to increase along both peeling directions, with the value of E along the peeling direction 1 being more sensitive to the change of angle. As a result, the adhesion enhancement along the two directions becomes more comparable in Model A, leading to weaker directional adhesion.

Finally, we comment on a few differences between the experiments and simulations. Firstly, the peeling condition applied in the finite element analysis was different from that used in the experiments. In the simulations, a fixed displacement is applied on the first few nodes on the top edge whereas during the peeling experiments, the angle between the force direction and the interface was kept at 90° . In the simulations, when the crack propagates in the peeling direction 2 along the vertical part of the interface, compressive contact is formed between the upper and lower surfaces resulting in the stored strain energy in the bulk material near the interface pattern. When the crack tip moves to the later R_{min} locations, the stored strain energy is released, leading to increase in $G_{pattern}$ and hence in R , as shown in Figure 5(b) and Figure 5(d). This strain energy penalty mechanism^[66] counteracts adhesion enhancement and as a result the E value along the peeling direction 2 is found to decrease with increasing crack length, as shown by the blue symbols in Figure 6(d) and Figure 6(e). Due to the asymmetric pattern, separation of the interface along the peeling direction 1 is not subjected to compressive surface contact and subsequent delayed strain energy release. Correspondingly, R decreases, as shown in Figure 5(a) and Figure 5(c), and E increases, as shown by the red symbols in Figure 6(d) and Figure 6(e), as the crack extends along the peeling direction 1. More evidence for this can be seen in Figure 6(c), which presents the numerical results for model B with the contact between the surfaces removed. Note that removing contact in the finite element analysis is a numerical treatment allowing the two surfaces to interpenetrate, which is physically unrealistic. However, this numerical exercise allows us to see the effect of the contact between the two surfaces. The results show that without the presence of

contact, the E value along the peeling direction 1 remains the same value, whereas the E value along the peeling direction 2 becomes zero throughout the entire interface. More discussion on this can be found in the **Supplementary Information**. During the 90° peeling in the experiments, the upper surface is completely separated from the lower one in the cracked region, and the strain energy penalty mechanism does not apply. Consequently, in the experiments the adhesion enhancement along the peeling direction 2 is larger than that along peeling direction 1 for both models, whereas from the simulations E in direction 2 is comparable to that in direction 1 for Model A. Secondly, in the experiments the deformation near the crack tip can be very large, which was difficult to simulate in the finite element analysis due to convergence issues. A relatively small fixed displacement boundary condition, i.e., $\delta_0 = 10 \mu\text{m}$, was intentionally applied in the numerical model so that the deformation near the crack tip becomes much smaller. Furthermore, the composite electrodes in commercial batteries are heterogeneous materials consisting of metal- or ceramic-like active materials, polymeric binders, and porous carbon black conductive matrix. The mechanical properties of composite electrodes are highly dependent on the packing density of the active material from the elementary powders and tortuosity of the surrounding medium. The mechanical properties of active materials may vary significantly with the state of charge, for example, elastic modulus of graphite increases by three folds upon lithiation. Numerical simulation based on realistic structures and properties of the composite electrodes remains a challenging task. Thus, in the numerical simulation the film was assumed to be of homogenous material with the Young's modulus and the Poisson's ratio of a typical PVDF binder. Lastly, the surfaces of the fabricated samples were not perfectly smooth due to fabrication tolerances. The above differences could explain the quantitative differences between the experimental and the numerical results. Nevertheless, the simulation results qualitatively agree with the experiments and provide additional insights into the mechanism of adhesion enhancement and directional adhesion achieved by the patterned interface.

3. Conclusion

Inspired by the controllable attachment and detachment ability of geckos' foot-hairs, the goal of this study is to design microscale near-surface architecture on the interface between the metallic current collector and the composite film of the electrode so that it displays controllable and directional adhesion, i.e., enhanced adhesion is obtained during its lifetime to cope with the substantial volume changes of the composite film upon intercalation and deintercalation, whereas during recycling, the composite film can be easily peeled off from the current collector in a certain direction. In this study, the simplest triangular pattern was tested, which successfully demonstrated a proof of concept that this technology is viable. In the future, it would be of high interest to explore more sophisticated patterns and the correlation between surface patterning with battery electrochemical performance. In addition, due to the constraint of our current fabrication method, the height of the surface pattern cannot be smaller than $20 \mu\text{m}$. If the design is implemented in real lithium-ion batteries, the micro-structures at the interface should be scaled down. These endeavors will be left as our future work.

As a simple, efficient, and low-cost approach, this study is the first application of structural adhesives for the development of high-performance easy-to-recycle batteries. This technology will potentially make a significant contribution to increasing the recyclability of lithium-ion batteries. The application of this technology can also be extended to other electronic products to avoid an ever-growing volume of electronic waste. The fundamental understanding on the interfacial adhesion and delamination mechanisms provides a scientific footing for the realization of next-generation easy-to-recycle electronics.

4. Experimental Section

Fabrication of Textured Surfaces: The 7075 grade aluminum alloy plates were purchased from ASM Aerospace Specification Metals (Pompano Beach, FL, USA). Micro-machining process of creating the patterned interfaces was performed by using a Fanuc RoboDrill α -D21MiA5 (Fanuc America, Pine Brook, NJ, USA) coupled with a high-speed spindle of up to 80,000 RPM. Then a Fanuc RoboCut 180is-WB (Fanuc America, Pine Brook, NJ, USA) mounted with a wire of diameter 100 μm was used for cutting the plates into smaller pieces. Totally 20 aluminum plates with patterned surfaces were fabricated, with ten for each pattern. Ten aluminum plates with flat surfaces were also fabricated, serving as a control. Non-contact surface measurements were carried on the textured surfaces by a Sensofar Plu Neox optical profiler (Sensofar, Barcelona, Spain). All the plates have the global dimension of 20 mm \times 10 mm \times 0.5 mm.

Fabrication of Lithium-Ion Battery Electrodes: The electrode fabrication process followed the previously published procedure.^[60-62] As-received $\text{LiNi}_{0.5}\text{Mn}_{0.3}\text{Co}_{0.2}\text{O}_2$ powder (NMC532) (particle size distribution D_{50} value approximately 11 μm and Brunauer–Emmett–Teller surface area approximately 0.3 m^2/g) (TODA America, Battle Creek, MI, USA), Denka carbon black (powder grade) (Denka, Tokyo, Japan), carboxymethyl cellulose (molecular weight approximately 250,000 g/mol and degrees of substitution approximately 0.9) (Sigma-Aldrich, St. Louis, MO, USA), Solef XPH-859 PVDF Latex (Solvay S.A., Brussels, Belgium), and Solef 5130 PVDF (Solvay S.A., Brussels, Belgium) were used for preparing NMC 532 electrodes. N-Methylpyrrolidone (NMP) (Sigma-Aldrich, St. Louis, MO, USA) was used as solvent. Electrode slurry was prepared by a planetary mixer (Ross Laboratory Mixers & Blenders, Hauppauge, NY, USA) and composite films were coated onto the aluminum plates with both patterned and flat surfaces by using a pilot-scale slot-die coater (Frontier Industrial Technology, Towanda, PA, USA). All the electrodes were not calendered, and the thickness of the composite film was approximately 50 $\mu\text{m} \pm 3 \mu\text{m}$. Thickness measurements were carried out with a digital micrometer (Marathon Watch, Richmond Hill, Ontario, Canada) with resolution of 1 μm . The thickness of the composite film was measured at 24 positions spread over the width and length of the electrode area.

90° Peeling Tests: The composite films were peeled off using a universal testing machine Instron 5882 (Instron, Norwood, MA, USA) with a force resolution of 1 mN according to the standard procedure ASTM D6862.^[63] The initial part of the composite film was manually peeled off and attached to an adhesive tape, and the remaining composite film was then peeled off at a constant rate of 0.7 mm/min. The angle between the force direction and the interface was kept at 90° during all the peeling tests. For each patterned interface, the composite film was peeled off along two different directions. The peel force F needed to peel the composite films from the aluminum

substrates was recorded. The peel energy was deduced from the peel force F as F/M_t with M_t being the width of the tape.

Acknowledgements

Congrui Jin thanks the support from the Research Foundation for the State University of New York through the Smart Energy Transdisciplinary Area of Excellence Program (TAE-16083098). Congrui Jin also thanks the support from the Small Scale Systems Integration and Packaging (S3IP) Center of Excellence, funded by New York Empire State Development's Division of Science, Technology and Innovation. Zhen Yang and Tian Tang acknowledge the financial support from Natural Sciences and Engineering Research Council of Canada. In addition, the support from the Karlsruhe Nano Micro Facility, a Helmholtz research infrastructure at Karlsruhe Institute of Technology, as well as Sirris's Microfabrication Application Laboratory, also known as Sirris's Small Laboratory, located in Seraing, Belgium, is gratefully acknowledged.

Conflicts of Interest

The authors declare no conflict of interest.

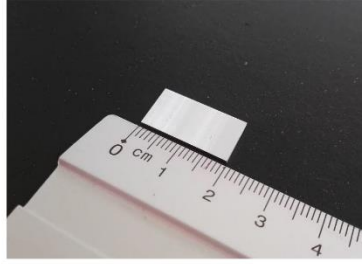
References

1. K. Ozawa, Lithium-ion rechargeable batteries with LiCoO₂ and carbon electrodes: the LiCoO₂/C system. *Solid State Ionics* 69 (1994) 212.
2. Y. J. Nishi, Lithium ion secondary batteries; past 10 years and the future. *J. Power Sources* 100 (2001) 101.
3. P. G. Bruce, B. Scrosati, J. M. Tarascon, Nanomaterials for rechargeable lithium batteries. *Angew. Chem. Int. Edit.* 47 (2008) 2930.
4. M. S. Whittingham, Lithium batteries and cathode materials. *Chem. Rev.* 104 (2004) 4271.
5. D. L. Wood, J. Li, C. Daniel, Prospects for reducing the processing cost of lithium ion batteries. *J. Power Sources* 275 (2015) 234.
6. X. Su, Q. Wu, X. Zhan, J. Wu, S. Wei, Z. Guo, Advanced titania nanostructures and composites for lithium ion battery. *J. Mater. Sci.* 47 (2012) 2519.
7. G. P. Hammond, T. Hazeldine, Indicative energy technology assessment of advanced rechargeable batteries. *Appl. Energy* 138 (2015) 559.
8. B. Scrosati, J. Garche, Lithium batteries: Status, prospects and future. *J. Power Sources* 195 (2010) 2419.
9. J. Li, C. Daniel, D. L. Wood, Materials processing for lithium-ion batteries. *J. Power Sources* 196 (2011) 2452.
10. M. Sun, X. Yang, D. Huisingh, R. Wang, Y. Wang, Consumer behavior and perspectives concerning spent household battery collection and recycling in China: a case study. *J. Clean. Prod.* 107 (2015) 775.
11. M. A. Delucchi, C. Yang, A. F. Burke, J. M. Ogden, K. Kurani, J. Kessler, D. Sperling, An assessment of electric vehicles: technology, infrastructure requirements, greenhouse-gas emissions, petroleum use, material use, lifetime cost, consumer acceptance and policy initiatives. *Philos. Trans. Ser. A* 372 (2014) 20120325.

12. J. B. Dunn, L. Gaines, J. Sullivan, M. Q. Wang, Impact of recycling on cradle-to-gate energy consumption and greenhouse gas emissions of automotive lithium-ion batteries. *Environ. Sci. Technol.* 46 (2012) 12704.
13. S. Ziemann, M. Weil, L. Schebek, Tracing the fate of lithium: The development of a material flow model. *Resour. Conserv. Recycl.* 63 (2012) 26.
14. D. Kushnir, B. A. Sanden, The time dimension and lithium resource constraints for electric vehicles. *Resour. Policy* 37 (2012) 93.
15. P. W. Gruber, P. A. Medina, G. A. Keoleian, S. E. Kesler, M. P. Everson, T. J. Wallington, Global lithium availability. *J. Ind. Ecol.* 15 (2011) 760.
16. J. Yan, R. F. Boehm, H.-X. Yang, Recycling of Lithium-ion Batteries, *Handbook of Clean Energy Systems*, John Wiley & Sons, Chichester, NY, USA, 2015.
17. C. Hoyer, K. Kieckhafer, T. S. Spengler, Technology and capacity planning for the recycling of lithium-ion electric vehicle batteries in Germany. *J. Bus. Econ.* 85 (2014) 505.
18. X. Zeng, J. Li, Spent rechargeable lithium batteries in e-waste: composition and its implications. *Front. Environ. Sci. Eng.* 8 (2014) 792.
19. S. Ziemann, A. Grunwald, L. Schebek, D. B. Müller, M. Weil, The future of mobility and its critical raw materials. *Rev. Metall.* 110 (2013) 47.
20. K. Richa, C. W. Babbitt, G. Gaustad, X. Wang, A future perspective on lithium-ion battery waste flows from electric vehicles. *Resour. Conserv. Recycl.* 83 (2014) 63.
21. L. Li, J. B. Dunn, X. X. Zhang, L. Gaines, R. J. Chen, F. Wu, K. Amine, Recovery of metals from spent lithium-ion batteries with organic acids as leaching reagents and environmental assessment. *J. Power Sources* 233 (2013) 180.
22. C. Herrmann, A. Raatz, S. Andrew, J. Schmitt, Scenario-based development of disassembly systems for automotive lithium ion battery systems. *Adv. Mater. Res.* 907 (2014) 391.
23. T. Zhang, Y. He, L. Ge, R. Fu, X. Zhang, Y. Huang, Characteristics of wet and dry crushing methods in the recycling process of spent lithium-ion batteries. *J. Power Sources* 240 (2013) 766.
24. J. Li, S. Zhong, D. Xiong, H. Chen, Synthesis and electrochemical performances of LiCoO₂ recycled from the incisors bound of Li-ion batteries. *Rare Metals* 28 (2009) 328.
25. C. Hanisch, W. Haselrieder, A. Kwade, Method for reclaiming active material from a galvanic cell, and an active material separation installation, particularly an active metal separation installation. European Patent, EP2742559B1, 2013.
26. C. Hanisch, W. Haselrieder, A. Kwade, Method for reclaiming active material from a galvanic cell, and an active material separation installation, particularly an active metal separation installation. Patent, WO/2013/023640, 2013.
27. C. Hanisch, T. Loellhoeffel, J. Diekmann, K. J. Markley, W. Haselrieder, A. Kwade, Recycling of lithium-ion batteries: a novel method to separate coating and foil of electrodes. *J. Clean. Prod.* 108 (2015) 301.
28. Z. Zhang, T. Zeng, Y. Q. Lai, M. Jia, J. Li, A comparative study of different binders and their effects on electrochemical properties of LiMn₂O₄ cathode in lithium ion batteries. *J. Power Sources* 247 (2014) 1.
29. M. H. T. Nguyen, E. S. Oh, Application of a new acrylonitrile/butylacrylate water-based binder for negative electrodes of lithium-ion batteries. *Electrochem. Commun.* 35 (2013) 45.

30. D. Chen, R. Yi, S. Chen, T. Xu, M. L. Gordin, D. H. Wang, Facile synthesis of graphene-silicon nanocomposites with an advanced binder for high-performance lithium-ion battery anodes. *Solid State Ionics* 254 (2014) 65.
31. H. C. Wu, E. Lee, N. L. Wu, T. R. Jow, Effects of current collectors on power performance of $\text{Li}_4\text{Ti}_5\text{O}_{12}$ anode for Li-ion battery. *J. Power Sources*, 197 (2012) 301.
32. Z. Zheng, Z. Wang, X. Song, S. Xun, V. Battaglia, G. Liu, Biomimetic nanostructuring of copper thin films enhances adhesion to the negative electrode laminate in lithium-ion batteries. *ChemSusChem* 7 (2014) 2853.
33. D. Reyter, S. Rousselot, D. Mazouzi, M. Gauthier, P. Moreau, B. Lestriez, D. Guyomard, L. Roue, An electrochemically roughened Cu current collector for Si-based electrode in Li-ion batteries. *J. Power Sources* 239 (2013) 308.
34. N. Zhang, Y. Zheng, A. Trifonova, W. Pfleging, Laser structured Cu foil for high-performance lithium-ion battery anodes. *J. Appl. Electrochemistry* 47 (2017) 829.
35. W. Pfleging, A review of laser electrode processing for development and manufacturing of lithium-ion batteries. *Nanophotonics* 7 (2018) 549.
36. Y. Zheng, H. J. Seifert, H. Shi, Y. Zhang, C. Kubel, W. Pfleging, 3D silicon/graphite composite electrodes for high-energy lithium-ion batteries. *Electrochimica Acta* 317 (2019) 502.
37. K. Autumn, A. M. Peattie, Mechanisms of adhesion in geckos. *Integr. Compar. Biol.* 42 (2002) 1081.
38. W. R. Hansen, K. Autumn, Evidence for self-cleaning in gecko setae. *Proc. Natl. Acad. Sci. USA* 102 (2005) 385.
39. A. Bietsch, B. Michel, Conformal contact and pattern stability of stamps used for soft lithography. *J. Appl. Phys.* 88 (2000) 4310.
40. B. Persson, S. Gorb, The effect of surface roughness on the adhesion of elastic plates with application to biological systems. *J. Chem. Phys.* 119 (2003) 11437.
41. S. Vajpayee, K. Khare, S. Yang, C.-Y. Hui, A. Jagota, Adhesion selectivity using rippled surfaces. *Adv. Funct. Mater.* 21 (2011) 547.
42. H. Shahsavan, B. Zhao, Conformal adhesion enhancement on biomimetic microstructured surfaces. *Langmuir* 27 (2011) 7732.
43. A. K. Singh, Y. Bai, A. Jagota, C.-Y. Hui, Adhesion of microchannel based complementary surfaces. *Langmuir* 28 (2012) 4213.
44. F. Cordisco, P. D. Zavattieri, L. G. Hector, A. F. Bower, Toughness of a patterned interface between two elastically dissimilar solids. *Eng. Fract. Mech.* 96 (2012) 192.
45. C. Jin, A. Jagota, C.-Y. Hui, Structure and energetics of dislocations at micro-structured complementary interface govern adhesion. *Adv. Funct. Mater.* 23 (2013) 3452.
46. C. Jin, K. Khare, S. Vajpayee, S. Yang, A. Jagota, C.-Y. Hui, Adhesive contact between a rippled elastic surface and a rigid spherical indenter: from partial to full contact. *Soft Matter* 7 (2011) 10728.
47. B. Bhushan, Biomimetics: lessons from nature—an overview. *Phil. Trans. Roy. Soc. A* 367 (2009) 1445.
48. A. Jagota, C.-Y. Hui, N. Glassmaker, T. Tang, Mechanics of bioinspired and biomimetic fibrillar interfaces. *MRS Bull.* 32 (2007) 492.
49. C.-Y. Hui, A. Jagota, L. Shen, A. Rajan, N. Glassmaker, T. Tang, Design of bio-inspired fibrillar interfaces for contact and adhesion - theory and experiments. *J. Adhes. Sci. Technol.* 21 (2007) 1259.

50. L. F. Boesel, C. Greiner, E. Arzt, A. del Campo, Gecko-inspired surfaces: a path to strong and reversible dry adhesives. *Adv. Mater.* 22 (2010) 2125.
51. A. M. Lees, J. Hardie, The organs of adhesion in the aphid *Megoura viciae*. *J. Exp. Biol.* 136 (1988) 209.
52. S. N. Gorb, The design of the fly adhesive pad: distal tenent setae are adapted to the delivery of an adhesive secretion. *Proc. Roy. Soc. London B* 265 (1998) 747.
53. T. Eisner, D. J. Aneshansley, Defense by foot adhesion in a beetle (*Hemisphaerota cyanea*). *Proc. Nat. Acad. USA* 97 (2000) 6568.
54. W. Federle, M. Riehle, A. S. G. Curtis, R. J. Full, An integrative study of insect adhesion: mechanics and wet adhesion of pretarsal pads in ants. *Integr. Compar. Biol.* 42 (2002) 1100.
55. M. K. Kwak, H. E. Jeong, W. G. Bae, H. S. Jung, K. Y. Suh, Anisotropic adhesion properties of triangular-tip-shaped micropillars. *Small* 7 (2011) 2296.
56. K. Autumn, M. Sitti, Y. A. Liang, A. M. Peattie, S. Hansen, S. Sponberg, T. W. Kenny, R. Fearing, R. J. Israelachvili, R. J. Full, Evidence for van der Waals adhesion in gecko setae. *Proc. Natl. Acad. Sci. USA* 99 (2002) 12252.
57. K. Autumn, A. Dittmore, D. Santos, M. Spenko, M. Cutkosky, Frictional adhesion: a new angle on gecko attachment. *J. Exp. Biol.* 209 (2006) 3569.
58. J. Lee, R. S. Fearing, Contact self-cleaning of synthetic gecko adhesive from polymer microfibers. *Langmuir* 24 (2008) 10587.
59. M. P. Murphy, B. Aksak, M. Sitti, Gecko-Inspired directional and controllable adhesion. *Small* 5 (2005) 170.
60. A. Davoodabadi, J. Li, Y. Liang, D. Wood, T. Singler, C. Jin, Analysis of electrolyte imbibition through lithium-ion battery electrodes. *Journal of Power Sources* 424 (2019) 193.
61. A. Davoodabadi, J. Li, Y. Liang, R. Wang, H. Zhou, D. Wood, T. Singler, C. Jin, Characterization of surface free energy of composite electrodes for lithium-ion batteries. *Journal of the Electrochemical Society* 165 (2018) A2493.
62. L. S. de Vasconcelos, R. Xu, J. Li, K. Zhao, Grid indentation analysis of mechanical properties of composite electrodes in Li-ion batteries. *Extreme Mech. Lett.* 9 (2016) 495.
63. ASTM Standard D 6862, Standard Test Method for 90 Degree Peel Resistance of Adhesives, ASTM International, West Conshohocken, PA, 2004.
64. M. Lamblet, E. Verneuil, T. Vilmin, A. Buguin, P. Silberzan, L. Leger, Adhesion enhancement through micropatterning at polydimethylsiloxane – acrylic adhesive interfaces. *Langmuir* 23 (2007) 6966.
65. Abaqus FEA (formerly ABAQUS) is a commercial software suite for finite element analysis and computer-aided engineering. For more details see *Abaqus 6.14 Analysis User's Guide*, Dassault Systèmes Simulia Corp., Providence, RI, USA, 2014.
66. R. Hensel, K. Moh, and E. Arzt, Engineering micropatterned dry adhesives: from contact theory to handling applications. *Advanced Functional Materials* 28 (2018) 1800865.



Two types of patterned surfaces were fabricated on aluminum plates.

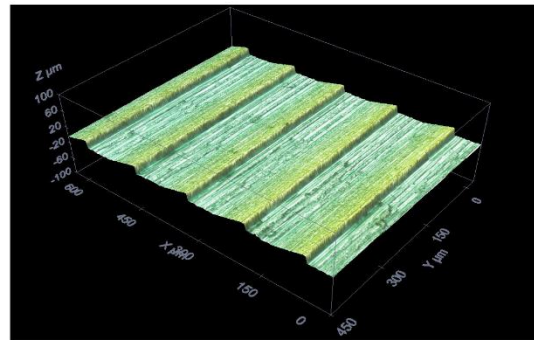
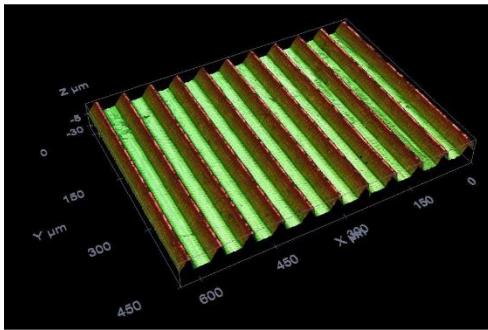
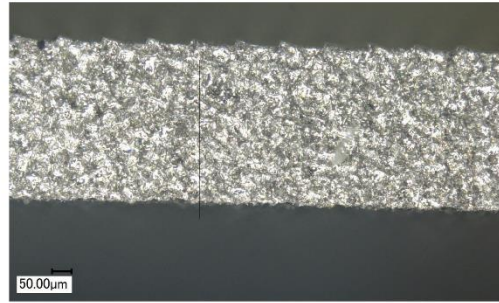
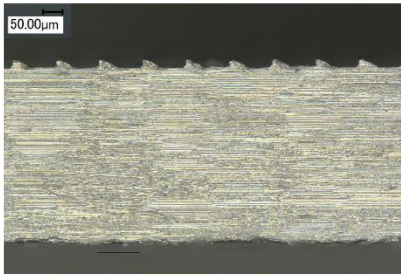
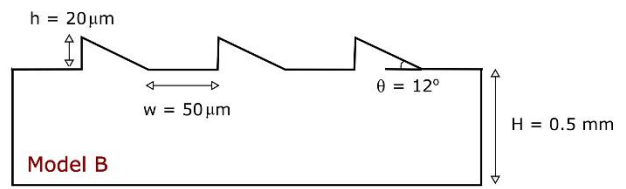
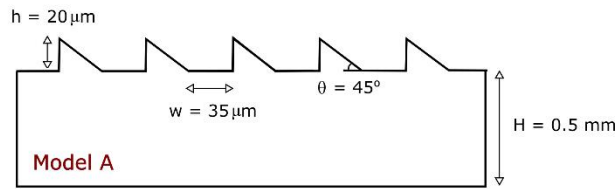


Figure 1. Inspired by the controllable attachment and detachment ability of geckos' foot-hairs, two types of patterned surfaces were fabricated on the aluminum plates, both of which contain asymmetric right triangles separated by flat regions, but with different geometrical parameters. Left panel: Model A; Right panel: Model B. For each model, a schematic drawing (not to scale) and a confocal microscope image are shown, respectively.

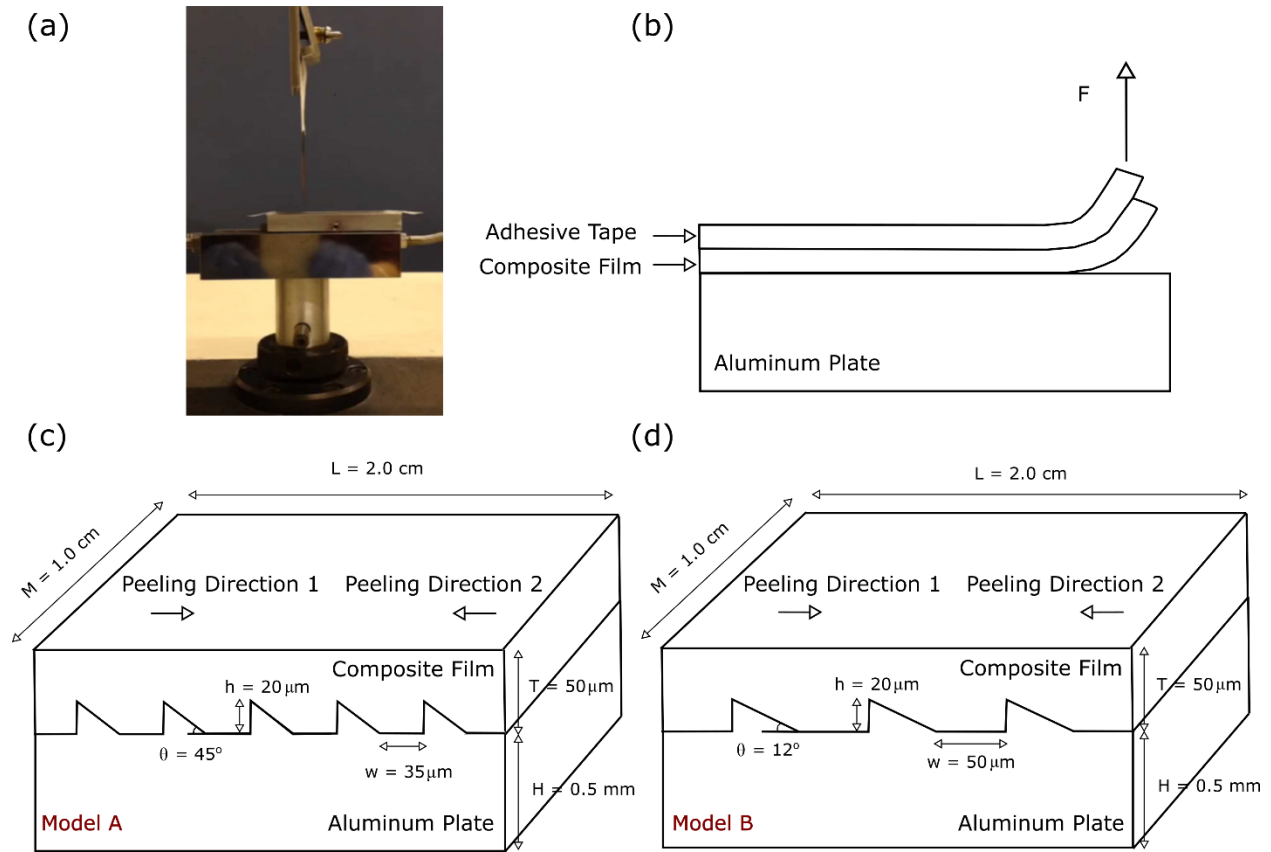


Figure 2. (a) To investigate the adhesion between the patterned current collectors and the composite films, the composite films were peeled off using a universal testing machine. An angle of 90° was maintained between the force direction and the interface during the peeling tests. (b) Schematics of the 90° peeling tests. For each patterned interface, (c) Model A and (d) Model B, respectively, the composite film was peeled off along two different directions.

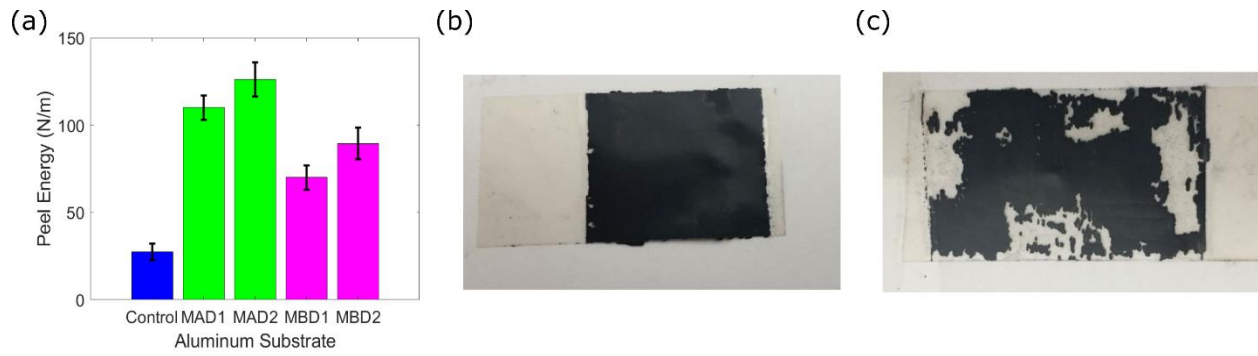


Figure 3. (a) The results of the peel energy are presented for Model A and Model B and each with two peeling directions, respectively. Error bars represent standard deviation from ten different tests. MAD1: Model A Direction 1; MAD2: Model A Direction 2; MBD1: Model B Direction 1; MBD2: Model B Direction 2. (b) The data were obtained from the tests in which the composite film was completely peeled off from the aluminum substrate. (c) If the composite film was not completely removed from the aluminum substrate, the data were considered as not useful for the analysis.

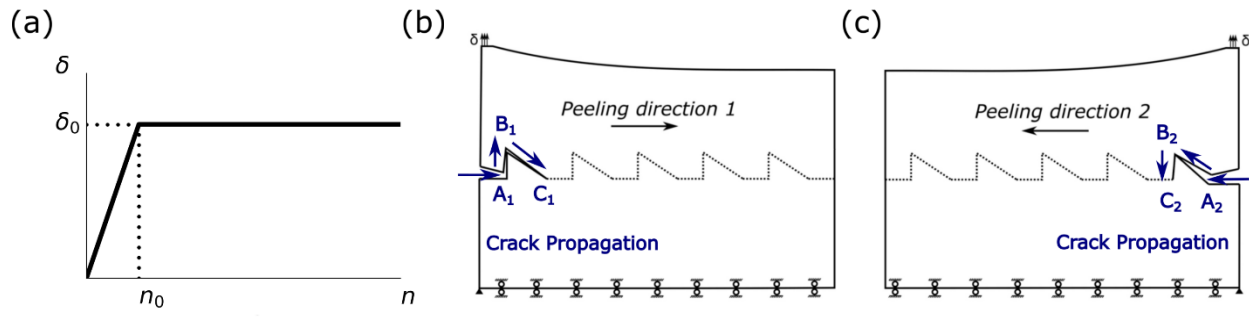


Figure 4. For the two numerical models, the same loading condition is applied where the first few nodes on the top edge is subjected to a fixed displacement boundary condition, and the bottom edge is fixed in a frictionless manner. (a): The displacement δ increases linearly from 0 to δ_0 as the numerical step n increases from 0 to n_0 , and afterwards δ remains constant. (b) and (c): Two opposite crack separation directions are examined numerically.

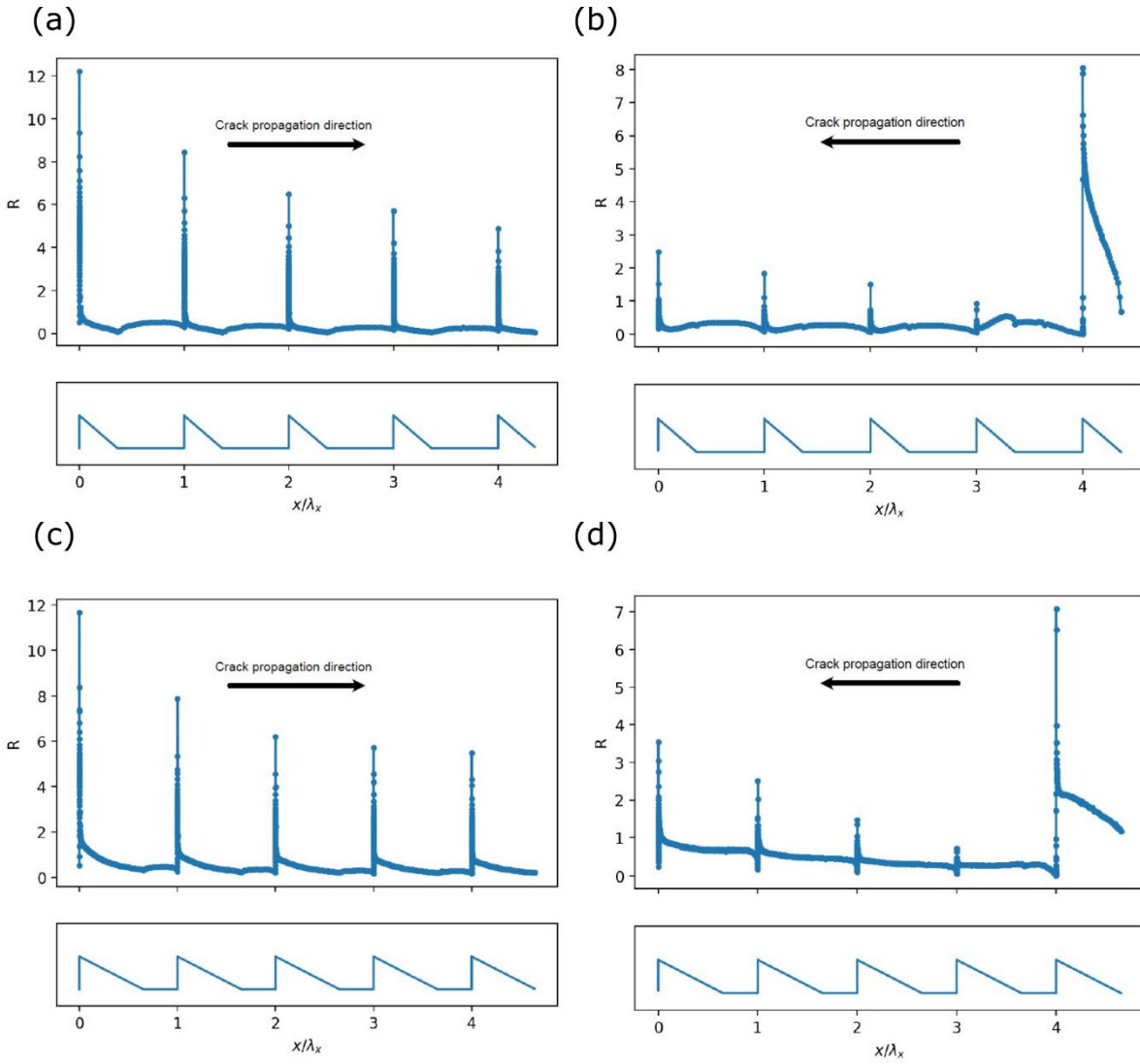


Figure 5. The energy release rate ratio R , defined as $G_{pattern}/G_{flat}$, plotted against the normalized apparent crack tip location x/λ_x in the patterned region. (a) Model A with peeling direction 1; (b) Model A with peeling direction 2; (c) Model B with peeling direction 1; and (d) Model B with peeling direction 2.

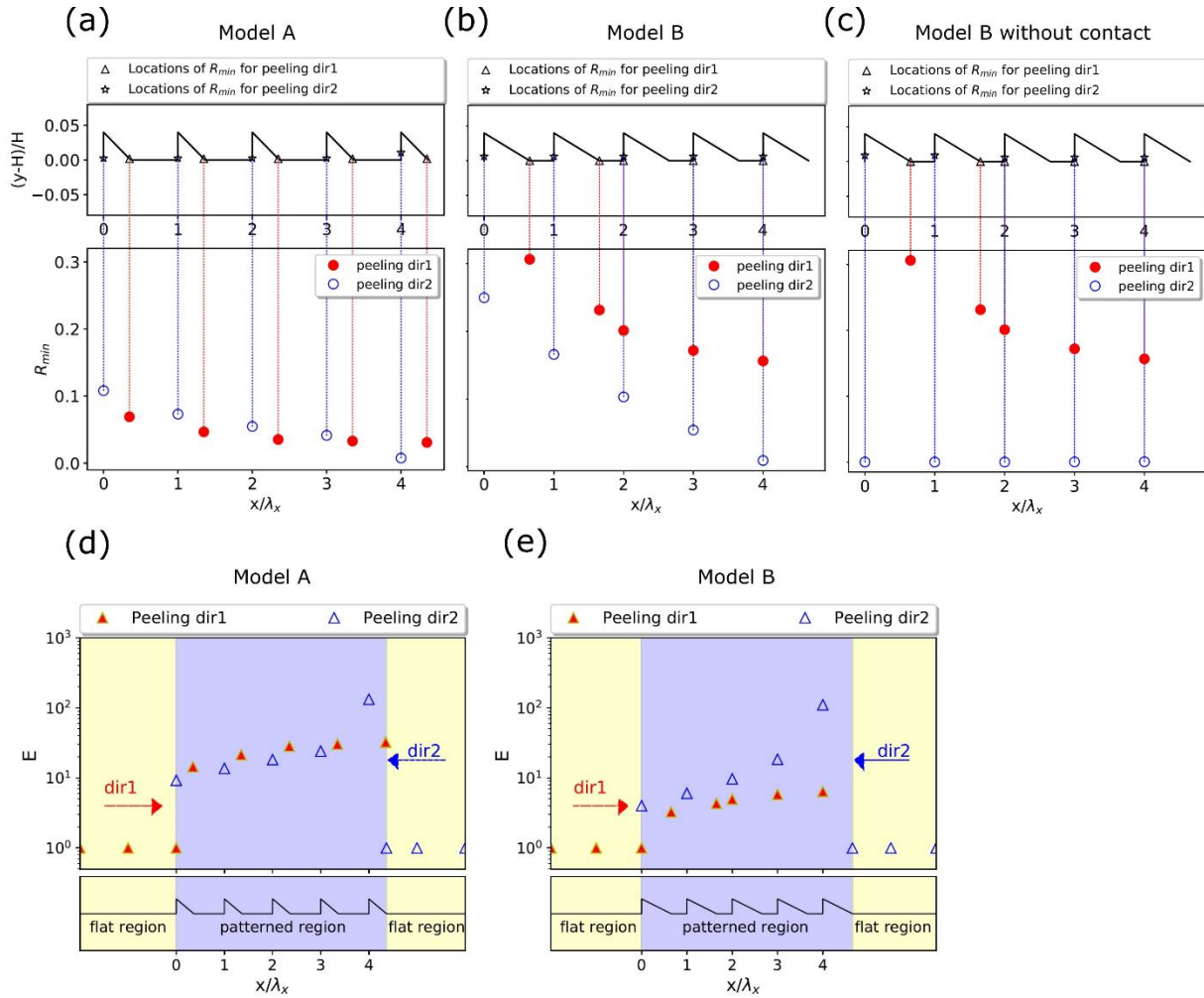


Figure 6. The plot of R_{min} , the minima of the R in each period of the pattern, against the normalized apparent crack tip location for the two models, (a) Model A and (b) Model B, respectively, each with two peeling directions. (c) The decreasing E value along the peeling direction 2 with increasing crack length was found to be due to a strain energy penalty mechanism, which is illustrated by the numerical results for model B with the contact between the surfaces removed. Adhesion enhancement factor E against the normalized apparent crack tip location for the two models, (d) Model A and (e) Model B, respectively, each with two peeling directions.

Table 1. Dimensions of the numerical simulation models (see **Figure 2** for the definition of the symbols).

Parameters	Dimensions in Model A	Dimensions in Model B
h	20 μm	20 μm
w	35 μm	50 μm
θ	45 deg	12 deg
L	1440 μm	1870 μm
T	50 μm	50 μm
H	500 μm	500 μm